

High-Rate Aqueous Aluminum-Ion Batteries Enabled by Confined Iodine Conversion Chemistry

Shuo Yang, Chuan Li, Haiming Lv, Xun Guo, Yanbo Wang, Cuiping Han, Chunyi Zhi,* and Hongfei Li*

Most reported cathode materials for rechargeable aqueous Al metal batteries are based on an intercalative-type chemistry mechanism. Herein, iodine embedded in MOF-derived N-doped microporous carbon polyhedrons ($I_2@ZIF-8-C$) is proposed to be a conversion-type cathode material for aqueous aluminum-ion batteries based on “water-in-salt” electrolytes. Compared with the conventional Al– I_2 battery using ionic liquid electrolyte, the proposed aqueous Al– I_2 battery delivers much enhanced electrochemical performance in terms of specific capacity and voltage plateaus. Benefitting from the confined liquid–solid conversion of iodine in hierarchical N-doped microporous carbon polyhedrons and enhanced reaction kinetics of aqueous electrolytes, the $I_2@ZIF-8-C$ electrode delivers high reversibility, superior specific capacity ($\approx 219.8 \text{ mAh g}^{-1}$ at 2 A g^{-1}), and high rate performance ($\approx 102.6 \text{ mAh g}^{-1}$ at 8 A g^{-1}). The reversible reaction between I_2 and I^- , with I_3^- and I_5^- as intermediates, is confirmed via *ex situ* Raman spectra and X-ray photoelectron spectroscopy. Furthermore, solid-state hydrogel electrolyte is employed to fabricate a flexible Al– I_2 battery, which shows performance comparable to batteries using liquid electrolyte and can be integrated to power wearable devices as a reliable energy supply.

1. Introduction

Ionic liquid $AlCl_3/[EMIM]Cl$ (1-ethyl-3-methylimidazoliumchloride) is the most widely used electrolyte for aluminum-ion batteries (AIBs) due to its wide range of electrochemical window and the reversible electroplating/stripping of Al. However, the environmental concerns, strict operating conditions, and corrosive properties of ionic liquids hinder their practical application.^[1] Recently, unlocking chemistry in rechargeable aqueous Al metal batteries provides impressive prospects regarding the cost, safety considerations, and ease of operation.^[2] One of the biggest obstacles that block the development of aqueous AIBs lies in the lack of proper cathode materials. To the best of my

S. Yang, C. Li, H. Lv, C. Zhi, H. Li
Songshan Lake Materials Laboratory
Dongguan, Guangdong 523808, China
E-mail: lihfh@sslslab.org.cn

S. Yang, C. Li, X. Guo, Y. Wang, C. Han, C. Zhi
Department of Materials Science and Engineering
City University of Hong Kong
Hong Kong 999077, China
E-mail: cy.zhi@cityu.edu.hk

 The ORCID identification number(s) for the author(s) of this article can be found under <https://doi.org/10.1002/smt.202100611>.

DOI: 10.1002/smt.202100611

knowledge, most reported cathodes for aqueous AIBs are enabled by the reversible insertion of Al^{3+} into cathode materials.^[3] The strong coulombic interactions attributed to the high charge density of Al^{3+} may lead to the structural collapse of the host material and diffusion limitation. Therefore, most intercalative-type cathodes exhibit poor electrochemical kinetics and unsatisfying long-term stability.^[4]

Iodine cathode with conversion–reaction mechanism possesses high theoretical capacity ($1040 \text{ mA h cm}^{-3}$) and high abundance in the ocean ($50\text{--}60 \text{ }\mu\text{g L}^{-1}$), making it an attractive alternative intercalative-type cathode.^[5] The main problems that hinder iodine application are the inferior electronic conductivity, poor thermal stability, and high dissolution of iodine species.^[6] Confining iodine into a porous conductive structure that may provide physical adsorption and chemical bonding can overcome the drawbacks.^[7]

Metal–organic frameworks (MOF) with high carbon and nitrogen contents were used as precursors to obtain nitrogen-doped porous carbon materials.^[8] The large surface area, uniformly distributed hierarchical porous, and high active site of MOF-derived carbon turn it into an ideal host for iodine species. Furthermore, carbon polyhedrons with high heteroatom concentration may provide a strong chemical adsorption ability of iodine, which could further improve the stability of iodine-based cathode.^[9]

Herein, for the first time, we investigated the reversible Al– I_2 conversion chemistry in the aqueous “water-in-salt” electrolyte (WISE) by embedding $\approx 30 \text{ wt}\%$ iodine in MOF-derived N-doped microporous carbon polyhedrons ($I_2@ZIF-8-C$). Compared with Al// $I_2@ZIF-8-C$ batteries using ionic liquid electrolyte, the aqueous batteries show higher specific capacity and discharge voltage. Besides, the carbon host with a unique hierarchical meso–micro porous structure, large surface area, and heteroatom doping not only can prohibit the dissolution of iodine species (I^- , I_3^- , I_5^-) by physical adsorption and chemical bonding but also can boost the reaction kinetics via 3D conducting skeletons. Attributed to the unique structure of the $I_2@ZIF-8-C$ cathode, the aqueous Al– I_2 battery delivers a desirable discharge capacity of $\approx 219.8 \text{ mAh g}^{-1}$ at 2 A g^{-1} . What’s more, the specific capacity remains to be $\approx 102.6 \text{ mAh g}^{-1}$ even at 8 A g^{-1} , suggesting an excellent rate capacity. Besides, the reversible

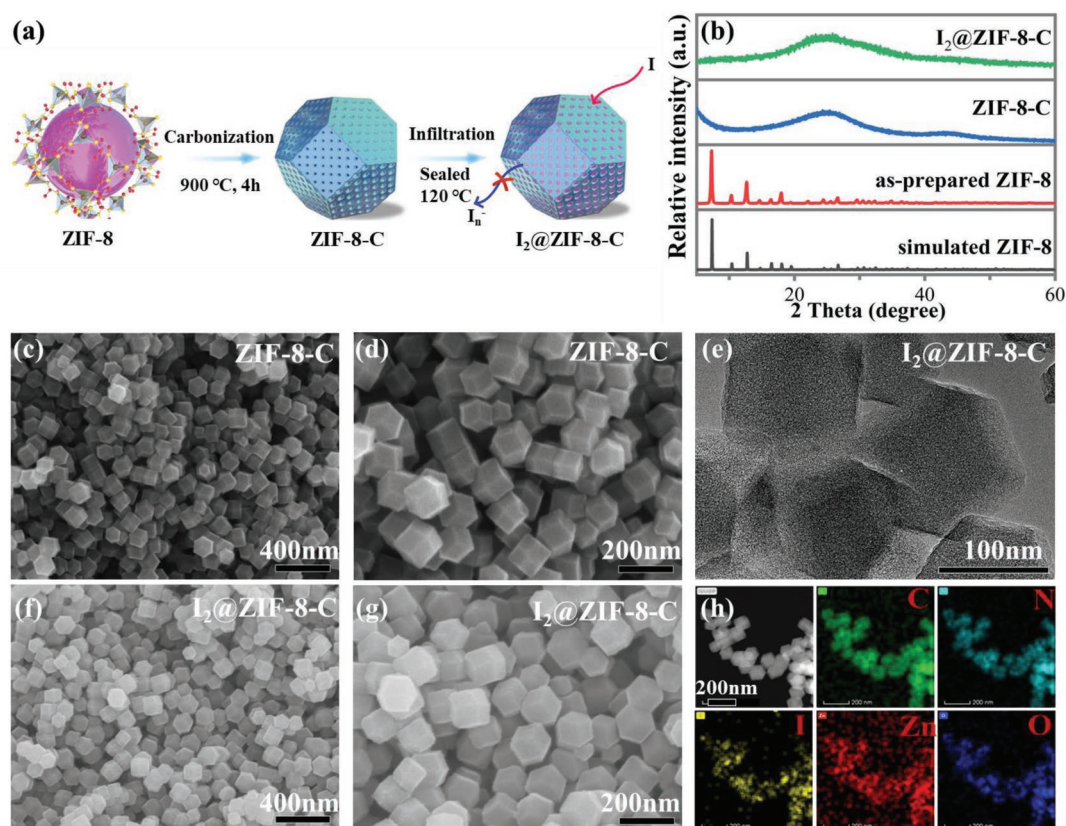


Figure 1. a) Schematic illustration of the synthesis process of $I_2@ZIF-8-C$. b) XRD patterns of ZIF-8, ZIF-8-C, and $I_2@ZIF-8-C$. c, d) SEM images at different magnifications of ZIF-8-C. e) TEM image, f, g) SEM images at different magnification, and h) EDS mapping of $I_2@ZIF-8-C$.

reaction between I_2 and I^- during the charge–discharge process was investigated by exploiting ex situ Raman spectra and X-ray photoelectron spectroscopy (XPS), which is assumed to be divided into three steps, with I_5^- and I_3^- as intermediate. A flexible aqueous solid-state Al– I_2 battery was subsequently fabricated by developing a polyacrylic acid (PAA) electrolyte, demonstrating its great potential in flexible and wearable applications. This study helps to inspire the exploration of conversion-type cathode materials for aqueous AIBs.

2. Results and Discussion

Figure 1a. illustrates the synthesis process of $I_2@ZIF-8-C$. First, the N-doped porous carbon polyhedron was prepared by directly carbonizing the zeolitic imidazolate framework (ZIF-8) under Ar flow at 900 °C. After that, iodine was loaded into the porous structure via a facile “melt-diffusion” process.^[10] According to the X-ray diffraction (XRD) patterns (Figure 1b), the diffraction peaks corresponding to the ZIF-8 crystal disappear after heat treatment, while two broad peaks at $\approx 25^\circ$ and 45° can be observed. The evolution of diffraction peaks is attributed to the decomposition of organic ligands and the formation of amorphous porous carbon.^[11] After iodine (≈ 30 wt%) is loaded into the conductive carbon host, no diffraction peak of iodine is observed in the XRD pattern, implying the good confinement of iodine within the meso–micro porous structure.^[12] Figure 1c, d shows the SEM images of MOF derived carbon polyhedron

(ZIF-8-C). The as-prepared ZIF-8-C nanoparticles with rhombic dodecahedra shape are similar to the pristine ZIF-8 crystal (Figure S1a, b, Supporting Information), indicating no significant morphology change during the carbonized process. After loading iodine into the porous structure, no distinct particles are observed outside ZIF-8-C (Figure 1f, g). This result further demonstrated the good confinement of iodine throughout the conductive carbon matrix rather than the outmost surface only.

TEM observation was operated to further study the detailed structure of ZIF-8-C. As shown in Figures S1 and S2, Supporting Information, in contrast with ZIF-8 showing deeper contrast, the TEM images of ZIF-8-C exhibit lighter contrast and numerous nanovoids distributed over the polyhedral, which may be attributed to the decomposition of light elements (C, N, and O). According to the energy dispersive spectrometer (EDS) mapping of ZIF-8-C (Figure S2d, Supporting Information), the C, N, O, and Zn elements distribute uniformly in the carbon matrix, indicating the transformation of ZIF-8 into nitrogen-rich carbon. The Zn content in ZIF-8-C is much lower than that in ZIF-8 (Figure S3a, b, Supporting Information) owing to the vapor of Zn at high temperatures. After iodine is loaded into the porous conductive matrix, the $I_2@ZIF-8-C$ nanoparticles retain their original polyhedral morphology (Figure 1e). At the same time, the I element is also observed in the EDS mapping (Figure 1h), suggesting the successful loading of iodine. It is noted that the TEM observation was operated in high-vacuum conditions after sonicating the $I_2@ZIF-8-C$ sample in water. As a result, the iodine content is relatively low (≈ 9.61 wt%), which

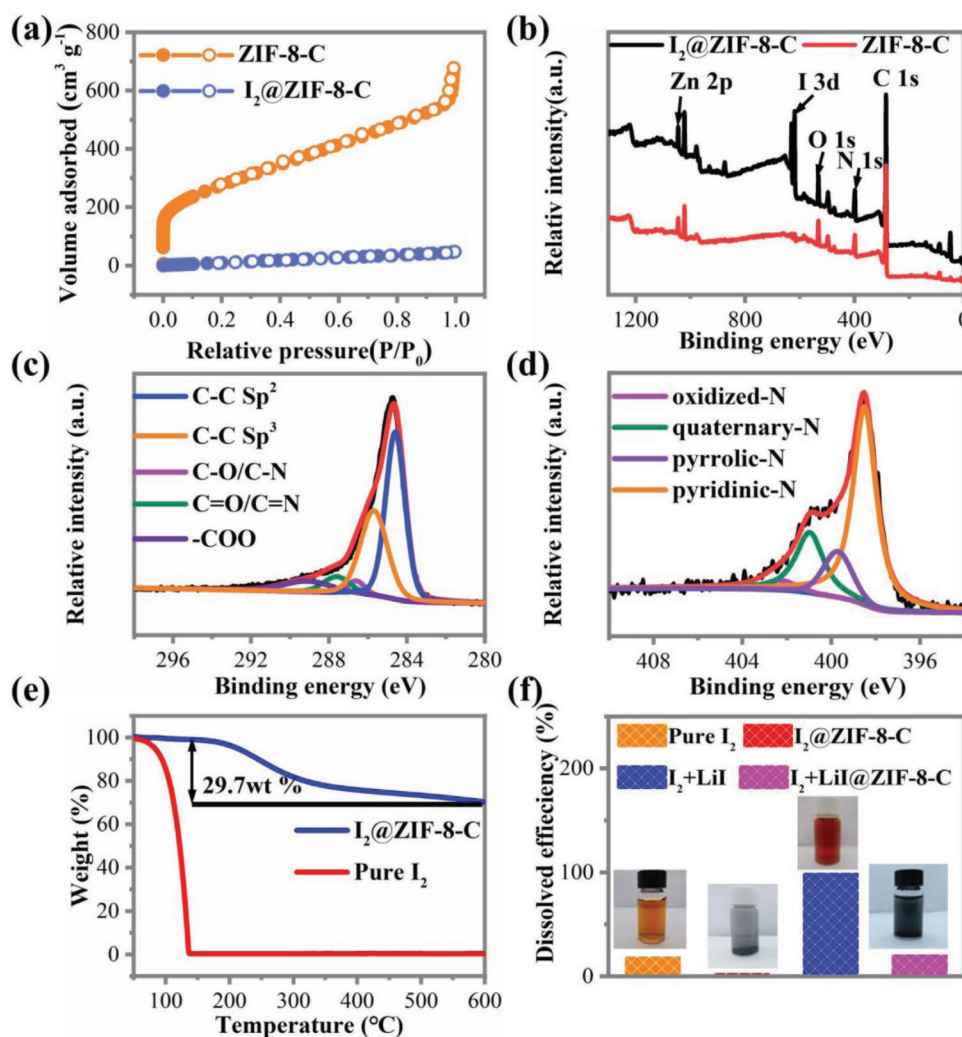


Figure 2. a) Nitrogen sorption isotherms and b) overall XPS spectra of ZIF-8-C and $I_2@ZIF-8-C$. XPS survey of c) C 1s and d) N 1s spectrum of $I_2@ZIF-8-C$. e) TG curves of ZIF-8-C and $I_2@ZIF-8-C$. f) Dissolved efficiency of different samples in water. The inset pictures are optical images of different dissolved samples.

means 67.9% of iodine was lost under such harsh conditions. (Figure S3c, Supporting Information).

The porous structure of ZIF-8-C and $I_2@ZIF-8-C$ was further characterized by N_2 adsorption–desorption measurements. As shown in **Figure 2a**, the ZIF-8-C sample exhibits a sharp adsorption slope of isotherm at the low relative pressure ($P/P_0 < 0.1$), suggesting the intrinsic micropore characteristic.^[11] The corresponding pore size distribution analysis further confirms the presence of micropores with a size centered at ≈ 1.7 nm (Figure S4, Supporting Information), which favors iodine adsorption. After loading iodine into the ZIF-8-C, the decreased peak intensities of the size distribution (Figure S4, Supporting Information) and specific surface area (from ≈ 975 to 89 $m^2 g^{-1}$) prove the successful confinement of iodine.

XPS measure was carried out to investigate the surface chemical states. It can be seen in the overall spectra of ZIF-8-C (Figure 2b) that there exist four elements C, N, O, and Zn. Additional peaks at around 618 and 630 eV corresponding to the I element are observed for the $I_2@ZIF-8-C$ sample, suggesting

the successful introduction of iodine.^[13] The High-resolution C 1s XPS spectrum of $I_2@ZIF-8-C$ (Figure 2c) can be convoluted into five peaks. The two strong peaks centered at 284.6 eV and 285.6 eV are ascribed to the sp^2 -hybridized graphite-like carbon (C–C sp^2) and sp^3 -hybridized diamond-like carbon (C–C sp^3), respectively.^[14] The three peaks centered at 286.6, 287.6, and 289.3 eV are assigned to C–O/C–N, C=O/C=N, and O=C–O, respectively, attributed to the surface oxygen and nitrogen groups.^[15] Due to the spin-orbit coupling, the high-resolution N 1s XPS spectrum of $I_2@ZIF-8-C$ (Figure 2d) can be deconvoluted to four sub-peaks centered at 398.5 eV, 399.7 eV, 401.0 eV, and 402.3 eV, corresponding to pyridinic-N, pyrrolic-N, quaternary-N, and oxidized pyridinic-N, respectively.^[16] It is noted that the formation of pyridinic-N is related to the higher nitrogen content, as proved by the EDS results (Figure S3c, Supporting Information). The total N content was ≈ 9.87 at%, higher than many reported N-doped carbons.^[17] The nitrogen atom in conductive carbon has proved strong interaction to iodine with chemical adsorption, which favors iodine cathode stability.

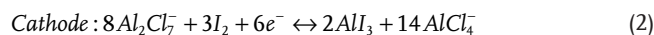
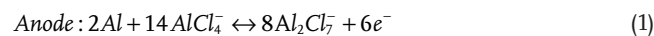
Figure S5, Supporting Information, shows the high-resolution Zn 2p XPS spectrum of I₂@ZIF-8-C. The fitting peaks centered at 1022.3 and 1045.5 eV are assigned to the formation of ZnO, while the peaks located at 1021.5 and 1044.8 eV are attributed to the Zn 2p_{1/2} and Zn 2p_{3/2}, respectively.^[12] Halide ions like I are typical soft Lewis bases, while there are soft Lewis acid groups on the surface of ZnO.^[18] Based on the theory of hard and soft acids and bases, the presence of electron-accepting centers on the ZnO surface is capable of adsorbing iodine species by forming a coordinated bond.^[19] As a result, the strong interaction between ZnO and iodine is conducive to restrain the dissolution of polyiodide, which is helpful for the cycling performance of Al–I₂ batteries.

The poor thermal stability of iodine and the high dissolution of polyiodides are two significant problems that hinder the development of iodine-based cathodes. Therefore, we compared the thermal stability of pure I₂ and I₂@ZIF-8-C composite using thermogravimetric (TG) measurements. As shown in Figure 2e, owing to the low sublimation temperature of pure I₂, a fast weight decrease is observed, and all the iodine is evaporated below 135 °C. On the other hand, the I₂@ZIF-8-C composite shows much better thermal stability with no noticeable weight loss before 175 °C. Besides, the I₂@ZIF-8-C composite exhibits a total weight loss of ≈29.7 wt%, closely matching its theoretical value of 30 wt%. Besides the thermal stability, the dissolution capability of iodine species was also investigated by dissolving different iodine-based samples into 10 mL H₂O and storing them for one day. As shown in Figure 2f, the aqueous solution turns brown immediately after adding pure I₂ or the mixture of LiI and I₂ into water, while the solution for I₂@ZIF-8-C and LiI+I₂@ZIF-8-C remains clear for more than one day. Next, the dissolved efficiency is calculated based on the iodine concentration in different solutions. For pure I₂ and LiI + I₂ samples, there is ≈19.3 wt% and ≈100 wt% iodine dissolved in the solution, respectively. After anchoring the I₂ and LiI + I₂ into the porous carbon matrix, the dissolved efficiency decreases to ≈3.4 wt% and ≈21.1 wt%, respectively, demonstrating the depressed iodine dissolution capability.

The aqueous Al–I₂ full cell was assembled by using a I₂@ZIF-8-C cathode, an Al metal anode, and WISE that composed of a mixture of 1 M AlCl₃ and 9 M lithium bis-trifluoromethanesulfonimide (LiTFSI) as electrolyte (Figure 3a). In this work, AlCl₃ was chosen to provide Al³⁺ while LiTFSI was added to widen the electrochemical windows of the electrolyte. However, if the concentration of LiTFSI is greater than 9 M, the electrolyte salt cannot be completely dissolved at room temperature (Figure S6, Supporting Information). The concentration of LiTFSI can be further increased by decreasing the content of AlCl₃ in the electrolyte. Nevertheless, the batteries based on the as-prepared electrolyte (0.5 M AlCl₃ + 9 M LiTFSI) show rather poor kinetics with inconspicuous redox peaks (Figure S7, Supporting Information).

Figure 3b compares the galvanostatic charge–discharge (GCD) curves of Al//I₂ batteries using AlCl₃/[EMIM]Cl electrolyte and WISE. The ionic liquid battery exhibits an initial discharge capacity of ≈97.8 mAh g^{−1} at a current density of 2 A g^{−1}, much lower than the aqueous battery (219.8 mAh g^{−1}). The higher specific capacity of the aqueous battery is related to the high ionic conductivities of aqueous electrolytes, thus boosting the fast reaction kinetics.^[20]

In addition to the better capacity performance, the aqueous Al–I₂ battery also displays higher discharge plateaus. The Al-ionic storage mechanism in the ionic liquid electrolyte can be summarized as:^[21a]



In nonaqueous electrolytes, I₃ is usually observed as an intermediate of the conversion reaction. However, the high current density may lead to high internal resistance and polarization of the electrode in the sluggish-kinetics ionic liquid electrolyte. As a result, I₂ may be transformed to I[−] directly, and the intermediate reaction cannot proceed, which further causes the low specific capacity and single plateau in ionic liquid electrolyte.^[21] As shown in Figure 3b, only one single discharge plateau is observed at ≈0.8 V for the ionic liquid electrolyte. In contrast, the aqueous battery shows three discharge plateaus at ≈1.6, 1.3, and 0.8 V. In Al–I₂ batteries based on AlCl₃/[EMIM]Cl electrolyte, AlCl₄[−] and Al₂Cl₇[−] anions instead of bare Al³⁺ act as charge carriers, which may require extra energy to break the strong Al–Cl bond and result in sluggish kinetics.^[22] Besides, the Al₂Cl₇[−] anion moves far away from the Al anode during the electrodeposition process, leading to severe battery polarization.^[23] These two processes can decrease the overall potential of the batteries and adversely affect the energy density. In aqueous electrolytes, Al³⁺ coordinates with OH groups and H₂O molecules to form [Al(OH₂)₆]³⁺ hydration shell, while Cl[−] tends to associate with Al³⁺ via partially sharing hydration shell.^[24] The unique solvation structure can help alleviate the impact of ionic liquid electrolytes and effectively reduce polarization behavior. Undoubtedly, the excellent capacity performance and the higher discharge potential make contributions to the total energy density.

Figure 3c exhibits the typical CV curves of aqueous Al//I₂@ZIF-8-C battery at various scan rates ranging from 5 to 20 mV s^{−1}. It delivers three reduction peaks centered around 1.7 V, 1.35 V, and 0.8 V during the cathodic scan (assigned to peak 1, peak 2, and peak 3, respectively), corresponding well with the GCD result. The redox current increases accordingly with the increased scan rate, while the shapes of CV curves remain unchanged greatly, indicating the fast-redox reactions between Al³⁺ and I₂. The electrochemical kinetics processes of Al//I₂@ZIF-8-C battery is further studied by calculating the *b* values according to the following equation:

$$i = av^b \quad (4)$$

where *a* and *b* represent adjustable constant parameters, *i* and *v* represent peak current and scan rate, respectively. According to the previous reports,^[25] the *b* value of 1.0 indicates a capacitive-limited process, whereas the *b* value of 0.5 represents a diffusion-controlled process. As shown in Figure S9, Supporting Information, the *b* values of peak 1, peak 2, and peak 3 are calculated to be 0.91, 0.50, and 0.73 (by plotting log(*i*) versus log(*v*)), respectively, indicating that the electrochemical process

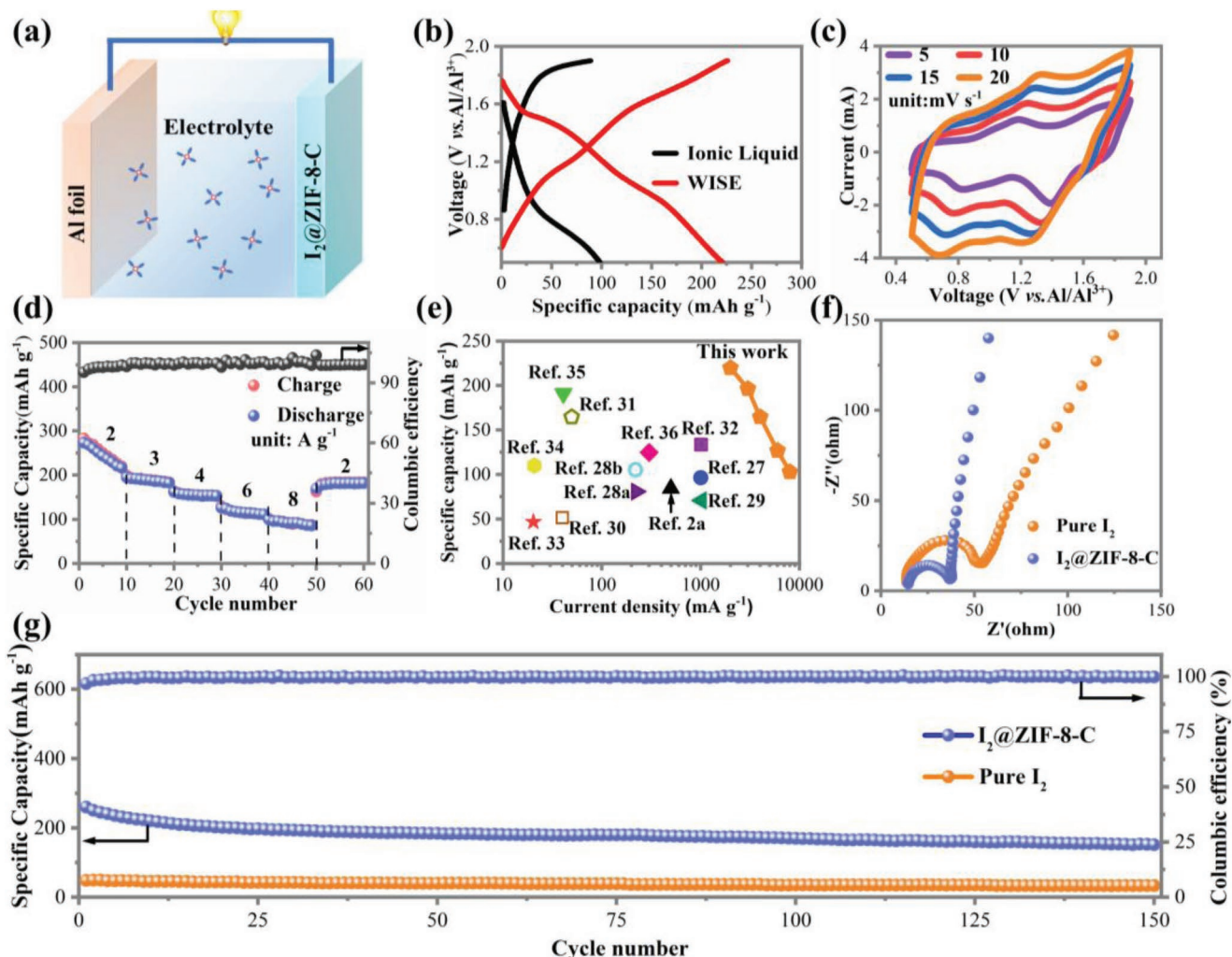


Figure 3. a) Schematic illustration of aqueous AIBs. b) GCD curves of Al//I₂@ZIF-8-C batteries using AlCl₃/[EMIM]Cl electrolyte and WISE. c) CV curves of aqueous Al//I₂@ZIF-8-C battery at various scan rates ranging from 5 to 20 mV s⁻¹. d) Rate performance of aqueous Al//I₂@ZIF-8-C battery. e) Specific capacity versus current density plot of our I₂@ZIF-8-C electrode and reported cathode for AIBs. f) EIS curves and g) cycling performances of pure I₂ and I₂@ZIF-8-C electrode at a current density of 2 A g⁻¹.

of I₂@ZIF-8-C cathode was influenced both by the diffusion-controlled process and surface-controlled capacitive process.

The rate performance of the aqueous Al//I₂@ZIF-8-C battery was also investigated (Figure 3d; Figure S10, Supporting Information). The Columbic efficiency is slightly lower at the first charge–discharge cycles owing to the side reactions like hydrogen evolution reaction and oxygen evolution reaction happening in aqueous electrolytes. In the first cycle, a thin passivation Al₂O₃ layer on surface Al anode will be formed, leading to higher resistance and more severe side effect.^[26] What's more, the current density increased with the increasing cycling number. Due to kinetic effects, the side reaction in the electrolyte can be restrained while cycling at higher current densities. The discharge capacities for aqueous Al//I₂@ZIF-8-C battery are 219.8, 196.2, 164.4, 129.5, and 102.6 mAh g⁻¹ at 2, 3, 4, 6, and 8 A g⁻¹, respectively. It is noted that such values surpassed many previously reported cathodes for AIBs, including Na₃V₂(PO₄)₃,^[27] I₂,^[28] graphite foam,^[29] V₂O₅/C,^[30] SnS porous film,^[31] and more, or aqueous cathodes including

graphite,^[32] KNHCF,^[33] K_yMnO₂,^[34] V₂O₅,^[35] α-MnO₂,^[2a] and Bir-MnO₂^[36] (Figure 3e; Table S1, Supporting Information). The superior rate capability is ascribed to the high ionic conductivity of the aqueous electrolyte and the unique hierarchical meso–micro porous structure of the carbon host that enlarges the active surface areas and enables fast ion diffusion. To further elucidate the improved reaction kinetics of the I₂@ZIF-8-C electrode compared with the pure I₂ electrode, electrochemical impedance spectroscopy (EIS) was operated. As shown in Figure 3f, both the plots present a quasi-semicircle in the high-frequency area representing the charge transfer resistance, and a slope in the low-frequency region indicating the ion diffusion resistance in the electrode. Compared with the pure I₂ electrode, the I₂@ZIF-8-C electrode exhibits much smaller charge transfer resistance and ion diffusion resistance, manifesting the enhanced electronic and ionic conductivity by the conductive porous carbon matrix.

Figure 3g compares the cycling performances of pure I₂ and I₂@ZIF-8-C electrodes at a current density of 2 A g⁻¹. The pure

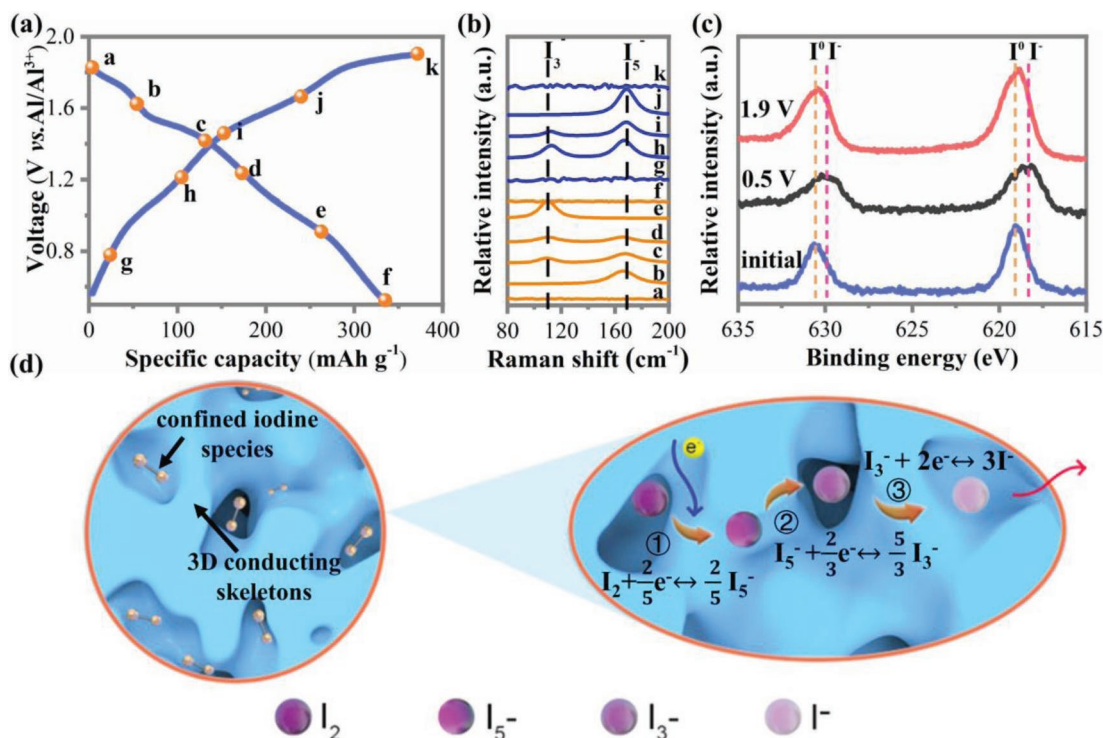


Figure 4. a) GCD curves of aqueous Al//I₂@ZIF-8-C for the second cycle at a current density of 1 A g⁻¹. The Raman analysis was performed at different points a–k. b) Raman spectra of I₂@ZIF-8-C electrode at different charge–discharge depths. c) 3d XPS of I₂@ZIF-8-C electrode at different charge–discharge states. d) The schematic description of the three-step electrochemical process of the I₂@ZIF-8-C electrode.

I₂ electrode exhibits a rather low specific capacity of ≈40 mA g⁻¹, far below its theoretical specific capacity of ≈211 mAh g⁻¹. On the other hand, the initial discharge capacity of the I₂@ZIF-8-C electrode is ≈259 mAh g⁻¹, slightly higher than the theoretical capacity of the iodine electrode, which may be attributed to the capacitance behavior of ZIF-8-C, as shown in Figure S11, Supporting Information. Although the I₂@ZIF-8-C electrode shows a fast capacity decay at the first 20 cycles (≈21.1%), a stable capacity of ≈162.0 mAh g⁻¹ is retained after 150 cycles, with a capacity fading of ≈0.25% per cycle. At the first several cycles, the capacity decay may be attributed to the small fraction of iodine species (I⁻, I₃⁻, etc.) dissolved in aqueous solution (Figure 2f). In the following cycles, the solid–liquid equilibrium between the adsorption iodine and dissolved iodine can be achieved, thus leading to the stabilized capacity.^[37] It is noted that the cycling performance exceeds most of the aqueous AIBs with Al anode reported so far (Figure S8, Supporting Information),^[2,36,38] demonstrating a great potential of high-capacity aqueous AIBs.

The enhanced cycling stability of the I₂@ZIF-8-C electrode compared with that of the pure I₂ electrode was ascribed to the enhanced conductivity, better thermal stability, and restrained solubility of iodine species triggered by the N-doped porous carbon polyhedrons. As shown in Figure S12, Supporting Information, carbon nanotubes (CNTs) instead of ZIF-8-C were also used as iodine's host material. Despite the higher electronic conductivity, the initial discharge capacity of the I₂@CNTs electrode is only ≈70 mAh g⁻¹. What's more, the capacity decays rapidly with increased cycling numbers, demonstrating the necessity of heteroatom doping and porous structure.

To further investigate the conversion chemistry of aqueous Al–I₂ batteries in WISE, the ex situ Raman was conducted at different charge–discharge depths for the second cycle (marked points in Figure 4a). Before discharging, no distinct peak is observed in the Raman spectra (Figure 4b), indicating the absence of polyiodide at the initial state. After discharging the battery at around 1.6 V, a clear peak between 170 and 160 cm⁻¹ assigned to the symmetric stretching mode of I₅⁻ emerges,^[39] indicating the transition from I₂ to I₅⁻. After that, the peak ascribed to the symmetric stretching mode of I₃⁻ (between 120 and 110 cm⁻¹) coexists with I₅ peak in the Raman spectra.^[13] As the discharging proceeds, the I₅ peak disappears and the intensity of I₃⁻ peak increases, implying that I₅ is reduced to I₃⁻. Finally, the I₃⁻ peak disappears at the end of discharge (from e to f), indicating the formation of I during the following discharging process. During the charging process, similar evolutions of Raman peaks are observed. It can be concluded that I⁻ is reversibly oxidized to I₂ after charging to 1.9 V. XPS was also operated to further characterize the redox state of the I element at fully discharged and fully charged states (Figure 4c). After discharging to 0.5 V, the I 3d peaks shift negatively as elemental iodine is reduced to the lower oxidation state, and AlI₃ is formed.^[40] Additionally, after charging to 1.9 V, the I 3d_{5/2} and I 3d_{3/2} peak shift back to 630.6 and 619.1 eV, respectively, further demonstrating the reversible conversion reaction. The reversible solid–liquid transition during charge–discharge processes demonstrates the excellent reversibility of the I₂@ZIF-8-C electrode, which makes it a promising candidate for rechargeable AIBs.

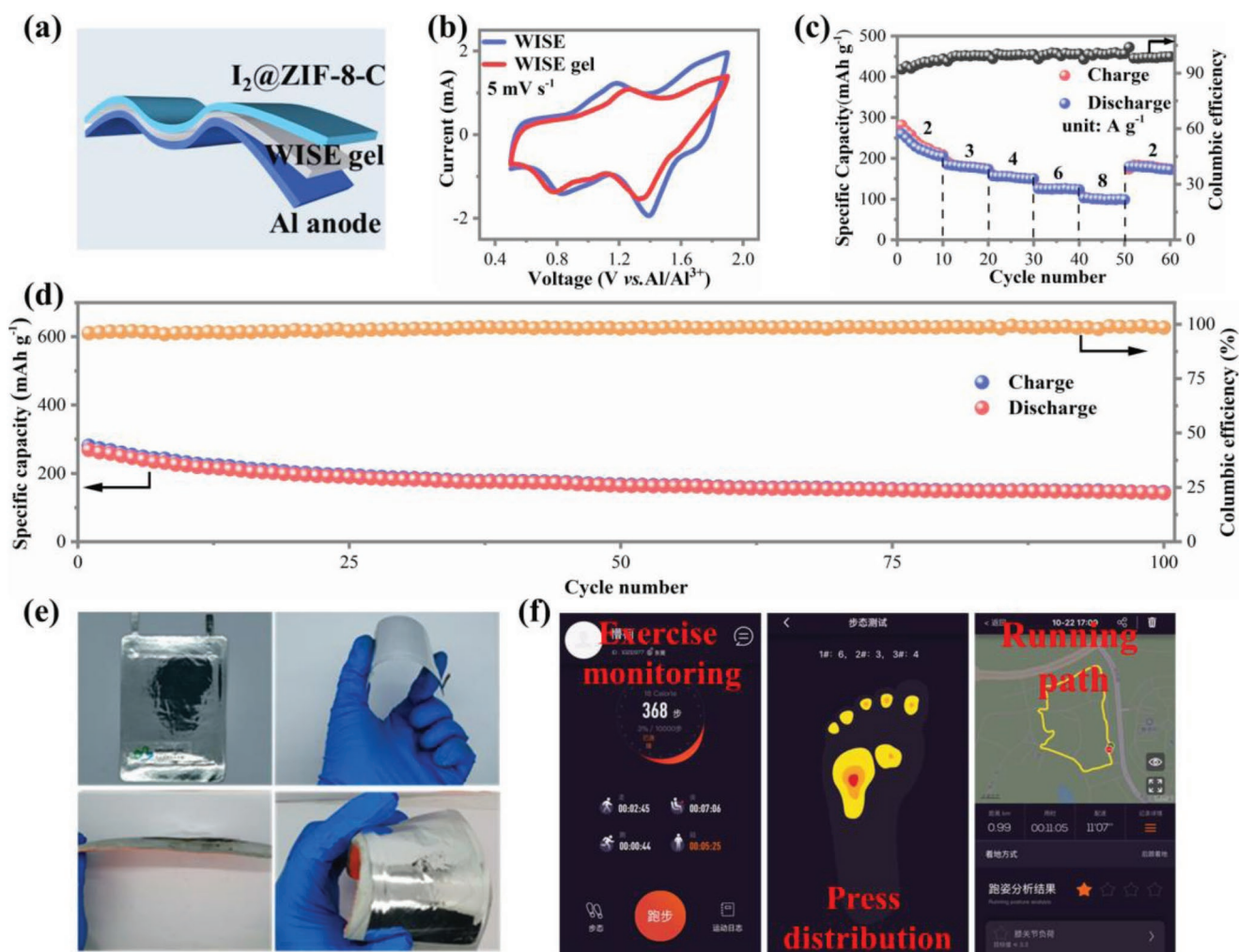


Figure 5. a) The schematic illustration of the flexible Al//I₂@ZIF-8-C battery. b) CV curves of the Al//I₂@ZIF-8-C battery with aqueous electrolyte and gel electrolyte. c) Rate performance, and d) cycling performance of the flexible Al//I₂@ZIF-8-C battery. e) Optical images of flexible Al//I₂@ZIF-8-C battery and AIB-powered smart insole. f) Exercise monitoring (left) by a smart insole powered by our flexible battery, pressure distribution (middle), and running path (right) obtained from the smart insole.

Figure 4d schematically illustrated the three-step electrochemical process of the I₂@ZIF-8-C electrode, which can be described as I₂ ↔ I₃⁻ ↔ I₃²⁻ ↔ I⁻. The carbon host with a unique hierarchical meso–micro porous structure can serve as abundant strong adsorption sites for soluble polyiodide species, while the 3D conductive carbon matrix with numerous interconnected nanopores can guarantee the fast ion and electrons transporting.

In order to develop flexible batteries for wearable devices, a WISE-based gel polymer electrolyte was fabricated by using the crosslinked PAA as a polymer matrix (details in Experimental section). As shown in Figure 5a, the solid-state battery was assembled with Al foil as the anode, I₂@ZIF-8-C as the cathode, and WISE gel as the electrolyte, respectively. The CV curves of the solid-state Al//I₂@ZIF-8-C battery are similar to that of the liquid-state ones (Figure 5b), which means the same redox chemistry happens by using gel electrolyte. Besides, the discharge capacities of solid-state batteries at various current densities (Figure 5c; Figure S13, Supporting Information) are much closed to that of the liquid-state battery. Specifically, the

discharge capacity at current densities of 2, 3, 4, 6, 8 A g⁻¹ are 205.8, 175.6, 150.8, 124.1, and 99.1 mA h g⁻¹, respectively. The slightly lower specific capacity may be attributed to higher charge transfer and ion diffusion resistances triggered by the interaction between hydrogel and solute.^[25a,41] Furthermore, the flexible battery shows reasonable stability with a remaining capacity of ≈145.6 mA h g⁻¹ after 100 cycles and a capacity decay of ≈0.46% per cycle (Figure 5d).

A potential application of solid-state batteries is to act as a flexible power system for wearable devices. Hence, three flexible batteries were connected in series to power a smart insole. As shown in Figure 5e, the solid-state batteries were sealed with ethylene acrylic acid film and polyethylene terephthalate hot gold foil to improve mechanical and waterproof properties. After connecting with the batteries, the real-time plantar information such as exercise monitoring, press distribution, and running path are recorded by the smart sole and sent to the mobile via Bluetooth (Figure 5f), demonstrating the flexible and wearable applications of Al//I₂@ZIF-8-C batteries.

3. Conclusion

In summary, iodine embedded in MOF-derived N-doped microporous carbon polyhedron was proposed to be the conversion-type cathode material for AIBs. The aqueous Al//I₂@ZIF-8-C battery delivered a higher specific capacity and discharge voltage by adopting the WISE with wide electrochemical windows than the ionic liquid counterpart. Besides, owing to the higher thermal stability and confined solid-liquid iodine conversion reactions triggered by the unique structure of ZIF-8 derived N-doped porous carbon, the aqueous Al//I₂@ZIF-8-C battery exhibited good cycling stability, superior specific capacity, and high rate performance (102.6 mAh g⁻¹ at 8 A g⁻¹). Ex situ characterizations and investigations revealed that the conversion chemistry of I₂ cathode could be divided into three steps, with I₅⁻ and I₃⁻ as intermediate: I₂ ↔ I₅⁻ ↔ I₃⁻ ↔ I⁻. Finally, the flexible aqueous AIBs were also prepared by adopting gel electrolyte, demonstrating high compatibility with AIBs at liquid state. Such aqueous AIBs with an aluminum anode and conversion-type cathodes may open avenues for further developing next-generation aqueous AIBs.

Supporting Information

Supporting Information is available from the Wiley Online Library or from the author.

Acknowledgements

S.Y., C.L., and H.L. contributed equally to this work. This research was supported by the National Natural Science Foundation of China (22005207), Guangdong Basic and Applied Basic Research Foundation (grant number: 2019A1515011819), and the National Key R&D Program of China under Project (2019YFA0705104).

Conflict of Interest

The authors declare no conflict of interest.

Data Availability Statement

Research data are not shared.

Keywords

aqueous Al-ion batteries, confined iodine, conversion chemistry, high rates

Received: June 8, 2021

Revised: July 30, 2021

Published online:

- S. Gu, Q. Zhang, Y. Bai, M. Li, Y. Yuan, H. Wang, X. Liu, Y. Yuan, N. Zhu, F. Wu, H. Li, L. Gu, J. Lu, *Nat. Commun.* **2019**, *10*, 73.
- [3] D. Yuan, J. Zhao, W. Manalastas, S. Kumar, M. Srinivasan, *Nano Mater. Sci.* **2020**, *2*, 248.
- [4] F. Wu, H. Yang, Y. Bai, C. Wu, *Adv. Mater.* **2019**, *31*, 1806510.
- [5] a) J. Xu, J. Ma, Q. Fan, S. Guo, S. Dou, *Adv. Mater.* **2017**, *29*, 1606454; b) L. Ma, Y. Ying, S. Chen, Z. Huang, X. Li, H. Huang, C. Zhi, *Angew. Chem., Int. Ed.* **2021**, *60*, 3791.
- [6] H. Tian, T. Gao, X. Li, X. Wang, C. Luo, X. Fan, C. Yang, L. Suo, Z. Ma, W. Han, C. Wang, *Nat. Commun.* **2017**, *8*, 14083.
- [7] a) K. Li, B. Lin, Q. Li, H. Wang, S. Zhang, C. Deng, *ACS Appl. Mater. Interfaces* **2017**, *9*, 20508. b) X. Li, N. Li, Z. Huang, Z. Chen, G. Liang, Q. Yang, M. Li, Y. Zhao, L. Ma, B. Dong, Q. Huang, J. Fan, C. Zhi, *Adv. Mater.* **2021**, *33*, 2006897.
- [8] L. Yang, X. Zeng, W. Wang, D. Cao, *Adv. Funct. Mater.* **2018**, *28*, 1704537.
- [9] D. Yu, A. Kumar, T. A. Nguyen, M. T. Nazir, G. Yasin, *ACS Sustainable Chem. Eng.* **2020**, *8*, 13769.
- [10] H. Tian, T. Gao, X. Li, X. Wang, C. Luo, X. Fan, C. Yang, L. Suo, Z. Ma, W. Han, *Nat. Commun.* **2017**, *8*, 14083.
- [11] L. Zhang, Z. Su, F. Jiang, L. Yang, J. Qian, Y. Zhou, W. Li, M. Hong, *Nanoscale* **2014**, *6*, 6590.
- [12] Z. Wu, J. Xu, Q. Zhang, H. Wang, S. Ye, Y. Wang, C. Lai, *Energy Storage Mater.* **2018**, *10*, 62.
- [13] Q. Zhao, Y. Lu, Z. Zhu, Z. Tao, J. Chen, *Nano Lett.* **2015**, *15*, 5982.
- [14] T. C. Nagaiah, A. Bordoloi, M. D. Sánchez, M. Muhler, W. Schuhmann, *ChemSusChem* **2012**, *5*, 637.
- [15] P. Chen, T.-Y. Xiao, Y.-H. Qian, S.-S. Li, S.-H. Yu, *Adv. Mater.* **2013**, *25*, 3192.
- [16] J. He, Y. Chen, W. Lv, K. Wen, C. Xu, W. Zhang, Y. Li, W. Qin, W. He, *ACS Nano* **2016**, *10*, 10981.
- [17] H. Wang, T. Maiyalagan, X. Wang, *ACS Catal.* **2012**, *2*, 781.
- [18] H. Zhang, J. Wang, H. Zheng, K. Zhuo, Y. Zhao, *J. Phys. Chem. B.* **2005**, *109*, 2610.
- [19] R. Pearson, *Usp. Khim.* **1971**, *40*, 1259.
- [20] a) G. Fang, J. Zhou, A. Pan, S. Liang, *ACS Energy Lett.* **2018**, *3*, 2480; b) C. Han, H. Li, Y. Li, J. Zhu, C. Zhi, *Nat. Commun.* **2021**, *12*, 2400.
- [21] a) M. Xing, Z. Zhao, Y. Zhang, J. Zhao, G. Cui, J. Dai, *Mater. Today Energy* **2020**, *18*, 100534; b) H. S. Ryu, Z. Guo, H. J. Ahn, G. B. Cho, H. Liu, *J. Power Sources* **2009**, *189*, 1179; c) K. Lu, Z. Hu, J. Ma, H. Ma, L. Dai, J. Zhang, *Nat. Commun.* **2017**, *8*, 527.
- [22] a) D. Wang, H. Lv, T. Hussain, Q. Yang, G. Liang, Y. Zhao, L. Ma, Q. Li, H. Li, B. Dong, T. Kaewmaraya, C. Zhi, *Nano Energy* **2021**, *84*, 105945; b) H. Yang, L. Yin, J. Liang, Z. Sun, Y. Wang, H. Li, K. He, L. Ma, Z. Peng, S. Qiu, C. Sun, H. M. Cheng, F. Li, *Angew. Chem., Int. Ed.* **2018**, *57*, 1898; c) Y. Zhang, S. Liu, Y. Ji, J. Ma, H. Yu, *Adv. Mater.* **2018**, *30*, 1706310.
- [23] C. Li, J. Patra, J. Li, P. C. Rath, M. H. Lin, J. K. Chang, *Adv. Funct. Mater.* **2020**, *30*, 1909565.
- [24] a) W. W. Rudolph, R. Mason, C. C. Pye, *Phys. Chem. Chem. Phys.* **2000**, *2*, 5030; b) E. Cauet, S. A. Bogatko, E. J. Bylaska, J. H. Weare, *Inorg. Chem.* **2012**, *51*, 10856.
- [25] a) H. Li, Q. Yang, F. Mo, G. Liang, Z. Liu, Z. Tang, L. Ma, J. Liu, Z. Shi, C. Zhi, *Energy Storage Mater.* **2019**, *19*, 94; b) X. Xu, J. Liu, Z. Liu, Z. Wang, R. Hu, J. Liu, L. Ouyang, M. Zhu, *Small* **2018**, *14*, 1800793; c) S. Yang, C. Li, Y. Wang, S. Chen, M. Cui, X. Bai, C. Zhi, H. Li, *Energy Storage Mater.* **2020**, *33*, 230; d) Y. Tang, X. Li, H. Lv, D. Xie, W. Wang, C. Zhi, H. Li, *Adv. Energy Mater.* **2020**, *10*, 200892.
- [26] J. Christensen, J. Newman, *J. Electrochem. Soc.* **2003**, *150*, A1416.
- [27] F. Nacimiento, M. Cabello, R. Alcántara, P. Lavela, J. L. Tirado, *Electrochim. Acta* **2018**, *260*, 798.
- [28] a) H. Tian, S. Zhang, Z. Meng, W. He, W.-Q. Han, *ACS Energy Lett.* **2017**, *2*, 1170; b) S. Zhang, X. Tan, Z. Meng, H. Tian, F. Xu, W.-Q. Han, *J. Mater. Chem. A* **2018**, *6*, 9984.
- [29] Y. Wu, M. Gong, M. C. Lin, C. Yuan, M. Angell, L. Huang, D. Y. Wang, X. Zhang, J. Yang, B. J. Hwang, *Adv. Mater.* **2016**, *28*, 9218.

[1] S. K. Das, S. Mahapatra, H. Lahan, *J. Mater. Chem. A* **2017**, *5*, 6347.

[2] a) Q. Zhao, M. J. Zachman, W. I. Al Sadat, J. X. Zheng, L. F. Kourkoutis, L. Archer, *Sci. Adv.* **2018**, *4*, eaau8131; b) C. Wu,

- [30] M. Chiku, H. Takeda, S. Matsumura, E. Higuchi, H. Inoue, *ACS Appl. Mater. Interfaces* **2015**, *7*, 24385.
- [31] K. Liang, L. Ju, S. Koul, A. Kushima, Y. Yang, *Adv. Energy Mater.* **2019**, *9*, 1802543.
- [32] W. Pan, Y. Wang, Y. Zhang, H. Y. H. Kwok, M. Wu, X. Zhao, D. Y. C. Leung, *J. Mater. Chem. A* **2019**, *7*, 17420.
- [33] Y. Gao, H. Yang, X. Wang, Y. Bai, N. Zhu, S. Guo, L. Suo, H. Li, H. Xu, C. Wu, *ChemSusChem* **2020**, *13*, 732.
- [34] J. Joseph, J. Nerkar, C. Tang, A. Du, A. P. O'Mullane, K. Ostrikov, *ChemSusChem* **2019**, *12*, 3753.
- [35] Q. Zhao, L. Liu, J. Yin, J. Zheng, D. Zhang, J. Chen, L. A. Archer, *Angew. Chem., Int. Ed.* **2020**, *59*, 3048.
- [36] S. He, J. Wang, X. Zhang, J. Chen, Z. Wang, T. Yang, Z. Liu, Y. Liang, B. Wang, S. Liu, *Adv. Funct. Mater.* **2019**, *29*, 1905228.
- [37] H. Pan, B. Li, D. Mei, Z. Nie, Y. Shao, G. Li, X. S. Li, K. S. Han, K. T. Mueller, V. Sprenkle, J. Liu, *ACS Energy Lett.* **2017**, *2*, 2674.
- [38] a) A. Zhou, L. Jiang, J. Yue, Y. Tong, Q. Zhang, Z. Lin, B. Liu, C. Wu, L. Suo, Y.-S. Hu, H. Li, L. Chen, *ACS Appl. Mater. Interfaces* **2019**, *11*, 41356; b) Z. Hu, Y. Guo, H. Jin, H. Ji, L.-j. Wan, *Chem. Commun.* **2020**, *56*, 2023; c) S. Kumar, R. Satish, V. Verma, H. Ren, P. Kidkhunthod, W. Manalastas Jr., M. Srinivasan, *J. Power Sources* **2019**, *426*, 151.
- [39] Z. Meng, H. Tian, S. Zhang, X. Yan, H. Ying, W. He, C. Liang, W. Zhang, X. Hou, W. Q. Han, *ACS Appl. Mater. Interfaces* **2018**, *10*, 17933.
- [40] P. M. Sherwood, *J. Chem. Soc., Faraday Trans. 2* **1976**, *72*, 1805.
- [41] Y. Wu, S. Joseph, N. Aluru, *J. Phys. Chem. B* **2009**, *113*, 3512.